01 Jan 2023

Using Catalysis To Control The Morphology And Stiffness Of Shape Memory Poly(isocyanurate-urethane) (PIR-PUR) Aerogels

A. B.M. Shaheen ud Doulah

Chandana Mandal

Hojat Majedi Far

Vaibhav A. Edlabadkar

et. al. For a complete list of authors, see https://scholarsmine.mst.edu/chem_facwork/3648

Recommended Citation

A. B. Shaheen ud Doulah et al., "Using Catalysis To Control The Morphology And Stiffness Of Shape Memory Poly(isocyanurate-urethane) (PIR-PUR) Aerogels," *ACS Applied Polymer Materials*, American Chemical Society, Jan 2023.
The definitive version is available at https://doi.org/10.1021/acsapm.3c00882

ACS APPLIED POLYMER MATERIALS

pubs.acs.org/acsapm Article

Using Catalysis to Control the Morphology and Stiffness of Shape Memory Poly(isocyanurate−urethane) (PIR−PUR) Aerogels

A. B. M. Shaheen ud Doulah, Chandana Mandal, Hojat Majedi Far, Vaibhav A. Edlabadkar, Rushi U. Soni, Stephen Y. Owusu, Nicholas Leventis,* and Chariklia Sotiriou-Leventis*

Cite This: ACS Appl. Polym. Mater. 2023, 5, 6851−6863 Read Online

ACCESS | Metrics & More | Article Recommendations | Supporting Information

ABSTRACT: A large array of anhydrous metal ions were tested as catalysts in the preparation of shape memory poly(isocyanurate−urethane) (PIR−PUR) aerogels from the reaction of 1,3,5-tris(6-isocyanatohexyl)-1,3,5-triazinane-2,4,6-trione (Desmodur N3300A: a well-known isocyanurate-based aliphatic triisocyanate) and triethylene glycol (TEG) in anhydrous acetonitrile. The reaction yielded wet gels that were dried into aerogels in an autoclave with supercritical fluid CO_2. The catalytic activity was mostly identified among CH_3CN-soluble salts (mainly chlorides) of third-row d-block elements from iron to zinc, group 13 elements from aluminum to thallium, as well as cadmium, bismuth, and tin. Tin (^{119}Sn) NMR indicated that the metal ion complexes with TEG, followed by reaction with the isocyanate. By using a fixed monomer concentration (20% w/w) and varying only the chemical identity and concentration of the catalysts, it was possible to demonstrate that the micromorphology of the resulting aerogels depended only on the gelation time. That is, for equal gelation times, the morphology was approximately the same, irrespective of the catalyst. For short gelation times (around 5 min or less), the aerogel frameworks were bicontinuous, changing to small spheroids at around 20 min and to large microspheres for gelation times around 75 min or more. Having obtained control over micromorphology, leaving other material properties such as density and porosity practically unaffected, it was possible to demonstrate that the bicontinuous structures of PIR−PUR aerogels can be up to 4 times stiffer and up to 2 times better thermal conductors than structures consisting of microspheres. This finding was attributed to the different widths of the neck zones between particles, noting that in bicontinuous morphologies, the neck diameters were almost equal to the particle diameters.

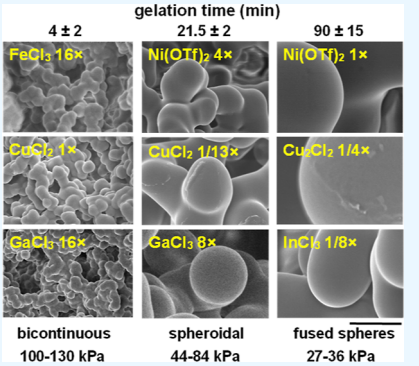

KEYWORDS: *aerogels, polyurethane, shape memory, morphology, bicontinuous, spheroidal*

1. INTRODUCTION

A hard-to-miss property of aerogels derived from isocyanates,[1] including polymer-crosslinked aerogels,[2] pristine polyurea,[3] polyurethane,[4] polyimide,[5] and polyamide aerogels,[6] is their remarkable mechanical strength.[7] Among those materials, aliphatic polyurea aerogels obtained from the reaction of water with an isocyanate,[8] specifically a isocyanurate-based triisocyanate trimer of hexamethylene triisocyanate (Desmodur N3300A), demonstrate a quite broad array of nanostructures,[9−11] and a significant recent finding was that their mechanical properties not only depend on the nanostructure, but most importantly they are not a single-valued function of the nanomorphology,[11] which, as it was speculated, was determined mainly by the mode of the phase separation of the polymer as it was formed:[12] Phase separation of solid nanoparticles gives nanoparticulate networks where individual particles may be either randomly distributed or organized in caterpillar-like structures of various aspect ratios. On the other hand, if the developing polymer is phase-separated as an "oily" phase that gets solidified later, the morphology of the aerogel skeletal networks can be quite diverse, ranging from thin nanofilaments to small solid microspheres embedded in nanofibers to larger solid microspheres with some fibers emanating from their surface. Those nano-/micromorphologies showed a correlation with increasing gelation time in the order just mentioned.[11]

Aliphatic polyurethane aerogels made by reacting the same aliphatic triisocyanate as the polyureas above with short aliphatic diol derivatives of ethylene glycol display diverse skeletal morphologies too, yet quite different from those of polyurea.[13−15] The common morphological denominator with the corresponding polyureas can be considered the presence of large, albeit now-bald microspheres. A completely different structural feature in these aliphatic polyurethane aerogels, not observed in the corresponding polyurea, was the occasional appearance of bicontinuous morphologies in which the solid and porous networks looked similar. It was proposed that all

Received: April 25, 2023
Accepted: July 27, 2023
Published: August 16, 2023

https://doi.org/10.1021/acsapm.3c00882
ACS Appl. Polym. Mater. 2023, 5, 6851−6863

these microstructures arise from the initial phase separation of an immiscible oily (i.e., liquid) mixture of oligomers, followed by solidification later as the reaction within the oily phase continues.[12]

This type of aliphatic polyurethane aerogels are superelastic materials with glass-transition temperatures in the range of 30−80 °C depending on the diol, ranging from ethylene glycol to tetraethylene glycol, and demonstrate a strong shape memory effect.[13−15] According to that effect,[16,17] these aerogels can be heated above their glass-transition temperature (T_g) and stretched to a temporary shape; they can retain that shape indefinitely if they are cooled, under the stretching load, to temperatures well below the glass-transition temperature; finally, they can return to their original shape if their temperature is increased back above T_g. Along these lines, it was discovered that the shape-recovery rate had a direct relationship with the elastic modulus (stiffness) via a Markus-type expression.[14] Fast shape-recovery rates are a desirable property for many practical applications, for example, in all sorts of actuation; therefore, stiffer shape memory materials were deemed more desirable.[13,18] Upon further inspection, it was noted that the highest elastic moduli were exhibited by bicontinuous microstructures, and the question became whether the higher stiffness of bicontinuous structures was due to that morphology or to other material properties associated with the particular aerogels that displayed that morphology. In our initial studies of those materials, bicontinuous micromorphologies were rather rare and their presence could be a function of any of the independent system variables as they were varied according to a statistical design-of-experiments model. Those system variables included the type and ratio of the diols in any particular formulation, the total monomer concentration in the sol, and the chemical identity of the solvent. All formulations used the same catalyst, dibutyltin dilaurate (DBTDL), and its mol ratio to the monomers (e.g., the triisocyanate) was kept constant. Further along the line, although bicontinuous morphologies were rare, it was noted that they resulted from formulations with higher monomer concentrations, and therefore, they were associated with faster gelling sols and higher density aerogels. On the other hand, the most common skeletal frameworks consisted of spheroidal particles. This type of frameworks was associated with lower monomer concentrations, therefore with slower gelling sols and lower density aerogels. Clearly then, although the higher stiffness of bicontinuous samples and the lower stiffness of spheroidal samples could be attributed to their morphologies, they could also very well be associated with their densities[19] or even with the different mixtures of diols used in their formulation.

At this point, it was reasoned that if bicontinuous morphologies are related only to the gelation time, then in order to deconvolute the role of the morphology on stiffness from other material properties, and therefore confirm or reject the morphology−stiffness hypothesis, all other system variables, like the sol concentration, should remain constant, and the only parameter that should be allowed to vary is the gelation time. The latter is related to the rate of polymerization, and therefore, it should be controllable through the catalyst: more active catalysts should bring about faster polymerization and therefore faster solidification of the phase-separated liquid mixture of oligomers, thus capturing the structural evolution at or closer to an ideal bicontinuous morphology; then, if those aerogels are stiffer, their higher moduli would be associated only with their morphology. Along this line of reasoning, a second way to control the rate of polymerization was by varying the catalyst concentration. According to the logic set forth here, irrespective of the catalyst and its concentration, the morphology (and stiffness) of the resulting aerogels should be similar to one another as long as they come from sols with similar gelation times. In other words, gelation time becomes a numerical proxy for the morphology of the polyurethane aerogels of this study, in the same conceptual context as the *K*-index did become previously the numerical proxy for the morphology of aliphatic polyurea aerogels derived from the same triisocyanate.[11]

Typical catalysts for urethane formation are based on metal ions, tertiary amines (e.g., 1,4-diazobicyclo[2,2,2]octane, abbreviated as DABCO), and selected organic acids. Among metal-based catalysts, the most common one has been DBTDL, which has been also effective in the reaction of isocyanates with polyether diols.[20] Therefore, as mentioned above, DBTDL was the catalyst of choice for the synthesis of shape memory polyurethane aerogels from Desmodur N3300A triisocyanate and short-chain glycols.[13−15] Non-tin-based metal catalysts include acetyl acetonate complexes of Cr^{3+}, Fe^{3+}, Cu^{2+}, Sn^{2+}, Mn^{2+}, Zr^{4+}, Hf^{4+}, In^{3+}, and Zn^{2+},[21] and they have also been effective with polyester diols.[20] In this study, we used anhydrous metal salts, mostly chlorides, and the criterion for their selection was their solubility in the gelation solvent (acetonitrile). Study of metal ion catalysis of the isocyanate−butanol reaction dates back in the mid-1960s.[22] It was reported that their effect varied based on steric factors of the isocyanate, and it was proposed that metal ions increased the electrophilic character of the isocyanate by coordinating with its oxygen or nitrogen. This mechanistic route does not seem to be in operation with the glycols of this study.

Based on the above, the triisocyanate (isocyanurate-based Desmodur N3300A triisocyanate), the diol (triethylene glycol, TEG), and their concentration (20% w/w) were kept constant throughout this study. The reaction rate, and thereby the gelation time, was varied from minutes to hours, both with the chemical identity of the metal ion catalyst and its concentration. The catalyst-to-isocyanate mol ratio of DBTDL (1:120) in our previous studies with related materials[13−15] was used as a point of reference. All other catalyst concentrations are referenced as multiples of that ratio. The resulting polymeric aerogels were classified as a special type of polyisocyanurate−polyurethane (PIR−PUR) materials, in which the isocyanurate ring was introduced as part of the isocyanate rather than formed in situ (Scheme 1). As supported by spectroscopic (FTIR and solid-state ^{13}C NMR) and CHN elemental analysis data, no identifiable amount of isocyanurate was formed as the result of side trimerization reactions of the NCO groups of Desmodur N3300A triisocyanate. In support of the view that gelation follows a phase separation of a liquid−oligomer path leading first to smaller spherules that coalesce to larger ones at longer gelation times,[23] it was confirmed that irrespective of the catalyst and its concentration, aerogels from similar gelation times had similar microstructures (e.g., consisting of similar size spherical particles). Bicontinuous morphologies were observed only in aerogels from very fast gelling sols (<10 min), supporting that these structures lied along the sequence of events that eventually furnished spherules. With a reliable approach to bicontinuous skeletal frameworks, it was possible to confirm that all bicontinuous structures are stiffer than those consisting

https://doi.org/10.1021/acsapm.3c00882
ACS Appl. Polym. Mater. 2023, 5, 6851−6863

Scheme 1. Preparation of PIR–PUR Aerogel for This Study

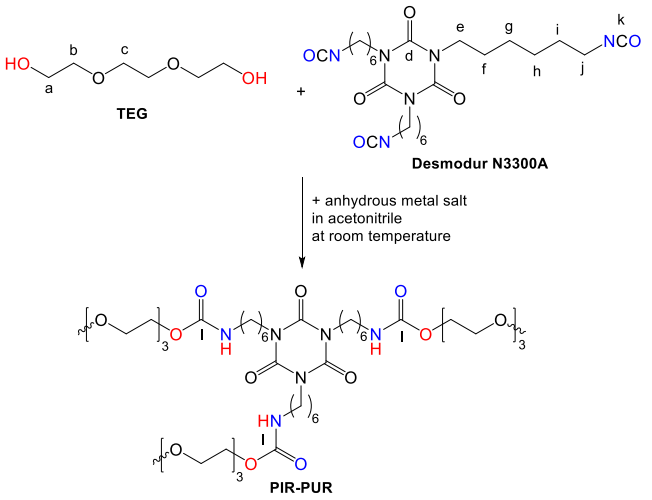

of spherical microparticles, and since the gelation time became a predictor of morphology, it was also possible to correlate stiffness with gelation time.

2. RESULTS AND DISCUSSION

2.1. Preparation of PIR–PUR Aerogels Using Anhydrous Metal Salts as Catalysts. The polyurethane aerogels for this study were obtained by drying polyurethane wet gels in an autoclave by first extracting the pore filling solvent with liquid CO_2 that was then converted to a supercritical fluid (SCF) and was vented off like a gas.[24] Referring to Scheme 1, Desmodur N3300A and TEG were introduced into the gelation process at their stoichiometric mol ratio of 2:3. The gelation solvent was acetonitrile, and the total monomer concentration (N3300A + TEG) was set at 20% w/w for all samples—all experiments. Thus, the only variables among all samples were the chemical identity and the concentration of the catalyst. Figure 1A shows the elements whose ions were tested as catalysts.

With the exception of $Cd(NO_3)_2$, $Tl(NO_3)_3$, and $Ni(OTf)_2$ (OTf: triflate), all other metallic ions were introduced as their anhydrous chloride salts. Stock solutions of these metal salts were prepared in anhydrous acetonitrile. TEG and N3300A were dissolved in acetonitrile separately. Predetermined amounts of each catalyst stock solution were added to each TEG solution. Then, the TEG/catalyst solutions were mixed with the triisocyanate solutions to form the sols as described in the Experimental Section. Color-coding in Figure 1A designates elements whose salts were considered, but they were insoluble in acetonitrile (yellow), elements whose salts were soluble but did not induce gelation (red) and elements whose salts did induce gelation (blue). $Cd(NO_3)_2$ and $BiCl_3$ were not fully soluble in acetonitrile, but they did dissolve in the presence of TEG. That posed experimental difficulties, so for comparison purposes, only one concentration of those salts was tested, the one referred to as "1×"—see below.

The catalytic activity as a function of the metal ion and its concentration were assessed by the gelation time, t_{gel}, measured from the time the triisocyanate solution was added to the TEG/metal ion solution. There are two ways to obtain t_{gel}. Using rheology in the oscillatory mode, t_{gel} is defined as the common crossing point of all tan δ (=loss modulus/storage

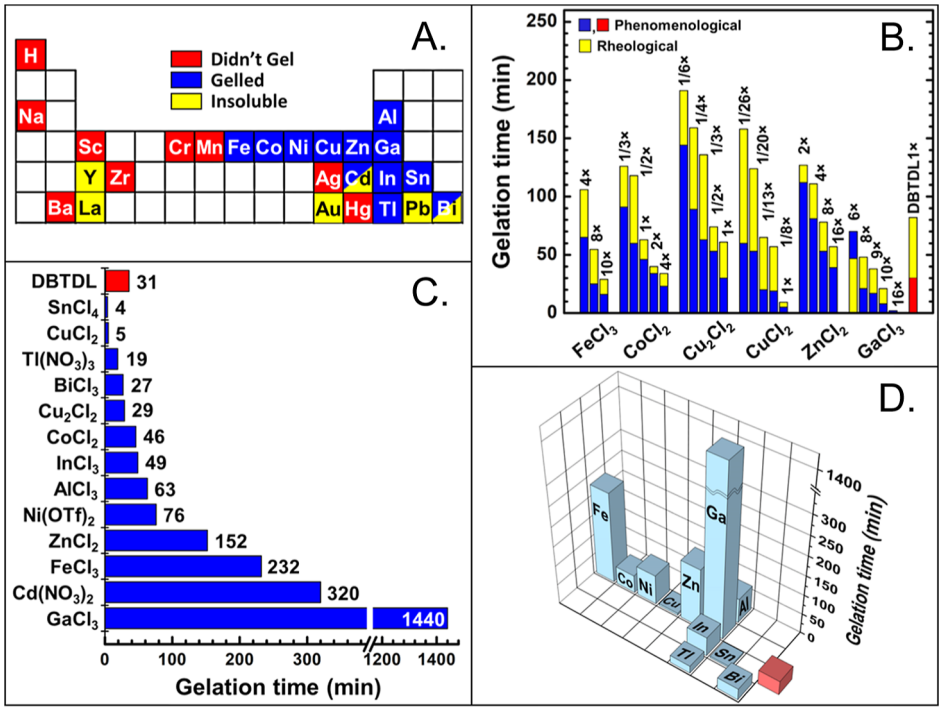

Figure 1. (A) Metals whose metal salts were tested for catalytic activity in the reaction of Scheme 1. (B) Comparison of rheological (yellow bars) versus phenomenological gelation times (blue and red bars) for selected salts at various concentrations, which are expressed as multiples for the reference concentration (1×) of DBTDL—see the text. (Note: all bars start from the bottom. Siting at the front, blue and red bars partially mask the yellow bars behind them. In all cases except one ($GaCl_3$, 6×), the rheological gelation times (yellow bars) were longer than the phenomenological gelation times.) (C) Comparison of the phenomenological gelation time of all catalysts at the reference concentration (1×). (D) Data from frame (C) plotted relative to the position of the elements in the periodic table. DBTDL is shown as a red box outside the frame.

https://doi.org/10.1021/acsapm.3c00882
ACS Appl. Polym. Mater. 2023, 5, 6851–6863

modulus) for all oscillatory frequencies employed in the experiment.[25−27] On the other hand, the phenomenological gelation time is taken as the point when the solution stops flowing. Figure 1B shows that in general, whenever both types of t_{gel} values were obtained, the phenomenological t_{gel} values were shorter than their rheological counterparts, but they followed the same pattern with the latter both within the same catalyst as a function of its concentration and across catalysts. The ensuing discussion is based on the phenomenological t_{gel} values as they were recorded for all catalysts at all concentrations. For the purposes of Figure 1B, the different molar concentrations of each catalyst are referred to as multiples of the standard concentration of DBTDL ([DBTDL] = 1.94 mM, referred to as 1× (see Table S1 of Appendix I in the Supporting Information), which was the concentration of DBTDL in the same monomer concentration sols (20% w/w) in our previous studies that comprised the impetus of this work.[13−15] In turn, Figure 1C shows the relative catalytic activity of all viable metal ions from Figure 1A, by comparing the gelation time of the common 20% w/w acetonitrile sol of this study with all metal ions at the same reference catalyst concentration (1×). According to Figure 1C, the most active catalyst was $SnCl_4$ (t_{gel} = 4 min), followed by $CuCl_2$ (t_{gel} = 5 min). The least active catalyst was $GaCl_3$ (t_{gel} = 24 h). Near-DBTDL catalytic activity at 1× (t_{gel} = 31 min) was displayed by Cu_2Cl_2 (t_{gel} = 29 min) and $BiCl_3$ (t_{gel} = 27 min). Finally, Figure 1D relates catalytic activity to the position of the corresponding elements in the periodic table. Catalytic activity was concentrated mainly across the first row of the d-block elements and the first group (number 13) of the p-block elements. Within the third-row d-block elements, t_{gel} decreased, and therefore, the catalytic activity increased from Fe^{3+} to Cu^{2+}, and then t_{gel} increased, and the catalytic activity decreased with Zn^{2+}. The catalytic activity decreased even further by moving toward gallium in group 13 of the p-block; in fact, $GaCl_3$ defined the global minimum of catalytic activity (t_{gel} = 24 h). Along group 13, $AlCl_3$ (t_{gel} = 63 min) showed an activity between $CoCl_2$ (t_{gel} = 46 min) and $Ni(OTf)_2$ (t_{gel} = 76 min), while on the other side of $GaCl_3$, $InCl_3$ (t_{gel} = 49 min) was more active than both $AlCl_3$ and $GaCl_3$, and the catalytic activity was increased further by moving to $Tl(NO_3)_3$, which was the third most active catalyst of all the metal salts tested (t_{gel} = 19 min), behind only $SnCl_4$ and $CuCl_2$.

The increase in catalytic activity from ferric chloride to $CuCl_2$ and the subsequent decrease with $ZnCl_2$ parallels the Irvin−Williams series of thermodynamic stability of the complexes of the corresponding ions.[28] That implies some sort of association of the starting materials with the catalyst. Using $SnCl_4$ as a proxy for all metal-salt based catalysts, and its diamagnetic NMR-active nucleus as a probe, we conducted a ^{119}Sn NMR study of the interaction of the reactants shown in Scheme 1 with $SnCl_4$ in CD_3CN—see Figure 2. A resonance from $SnCl_4$ was observed at −681.96 ppm versus external neat $Sn(CH_3)_4$. The chemical shift of $SnCl_4$ in pure form or in weakly interacting solvents (e.g., CS_2 or CH_2Cl_2) has been reported at around −150 ppm.[29] The large upfield chemical shift of $SnCl_4$ in acetonitrile implies strong interaction (complexation) with the solvent. When isocyanate was added to the $SnCl_4$ solution in a 1:1 mol/mol ratio, only a slight downfield change in the chemical shift was observed (to −680.60 ppm). On the other hand, when TEG was added to the $SnCl_4$ solution, in the same 1:1 mol/mol ratio, the ^{119}Sn resonance shifted significantly downfield (to −623.16 ppm)

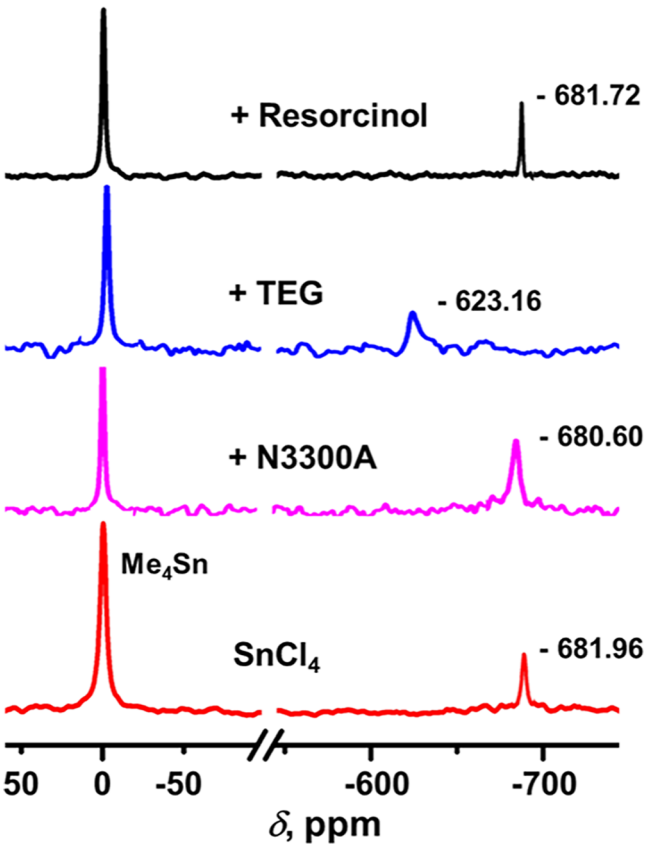

Figure 2. Liquid ^{119}Sn NMR of $SnCl_4$ in CD_3CN with several additives as shown in 1:1 mol/mol ratio. All spectra were referenced externally to pure tetramethyltin using a coaxial tube.

that is toward its chemical shift in pure diethyl ether (−606 ppm), as well as its chemical shift in weakly interacting CH_2Cl_2 containing either a 5 molar excess of diethyl ether (−599.4 ppm) or an equimolar amount of chelating dimethoxyethane (−550.0 ppm).[29] These facts considered together indicate that TEG interacted strongly with $SnCl_4$. On the other hand, an aromatic alcohol (resorcinol) did not cause any noteworthy shift of the ^{119}Sn resonance in acetonitrile (with resorcinol at 1:1 mol/mol ratio in solution: −681.72 ppm). Considering the structural analogy of TEG to chelating dimethoxyether,[29] it is speculated that the interaction of $SnCl_4$ with aliphatic TEG was assisted by its ability to chelate via five-membered rings. Assuming that TEG interacts with the other metal salts in the same general fashion provides a reasonable explanation for the assistance offered by TEG in dissolving the metal salts in acetonitrile, as noted in particular with $Cd(NO_3)_2$ and $BiCl_3$. Complexation of the metal ions with TEG puts the interaction with the isocyanate second in the sequence of events; thereby, without going into further speculation, the mechanism of urethane formation catalyzed by the metal ions of Figure 1A resembles the insertion mechanism of the DBTDL-catalyzed urethane formation[30] and explains adequately well the Irvin-Williams trend in the d-block elements of the third row, including the higher activity of harder Cu^{2+} over softer Cu^{+}. However, the behavior down group 13 of the p-block elements is more perplexing. Here, the softer metal ions (indium, thallium) were the most active catalysts, but the behavior of $GaCl_3$, being globally the least active catalyst, was surprising. Ga^{3+} is a hard Lewis acid, harder than Zn^{2+}, and following the logic of the Irvin−Williams series, $GaCl_3$ would be expected to

https://doi.org/10.1021/acsapm.3c00882
ACS Appl. Polym. Mater. 2023, 5, 6851−6863

be more active than $ZnCl_2$. Its behavior indicates that the interaction of the Ga(III) metal center with TEG is hindered, which in turn suggests either that $GaCl_3$ (in itself a soft acid) or its associative complex with acetonitrile does not interact strongly with TEG. Overall, in spite of the differences in their interaction with TEG or the isocyanate, the salts of the elements of Figure 1 comprise a set of catalysts with a widely variable activity toward the reaction of Scheme 1, with all other parameters remaining constant.

2.2. Chemical and General Materials Characterization of the PIR−PUR Aerogels. All PIR−PUR aerogels of this study were expected to have the same chemical composition, and that was supported by FTIR and solid-state CPMAS ^{13}C NMR spectroscopy, as well as by CHN elemental analysis data. Figure 3 shows the FTIR and the solid-state ^{13}C NMR spectra of all aerogels prepared with the catalyst concentrations

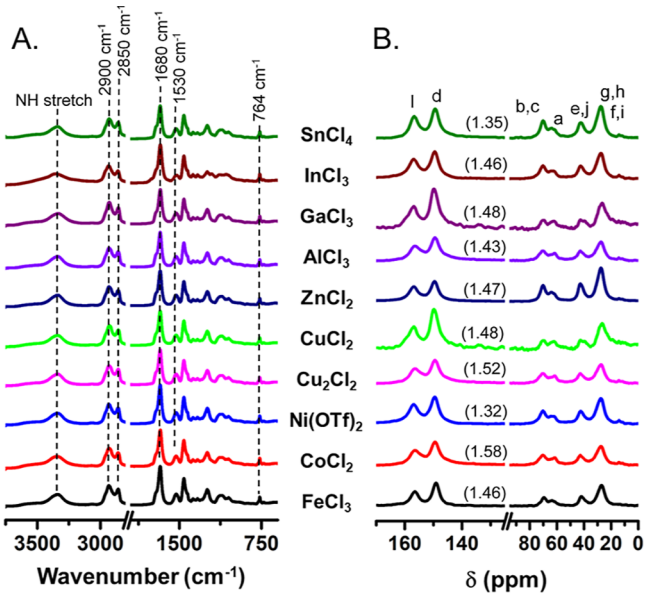

Figure 3. ATR−FTIR (A) and solid-state CPMAS ^{13}C NMR spectra (B) of polyurethane aerogels prepared according to Scheme 1 and catalyzed with the metal salts indicated in the figure. All spectra concern materials obtained with the corresponding catalysts set at the 1× concentration, except $GaCl_3$ (6×). The integrated isocyanurate-to-urethane ratios (d/l) are included in (parentheses) with each spectrum of part B. For other peak assignments, see Scheme 1.

set at 1×. All FTIR spectra (Figure 3A) were essentially identical to one another and were dominated by the isocyanurate carbonyl stretch near 1680 cm^{-1}. The 2300−2000 cm^{-1} region was clean of any unreacted N=C=O stretch. The free urethane carbonyl stretch was observed as a 1729 cm^{-1} shoulder of the intense isocyanurate absorption. H-bonded urethane carbonyl groups would appear at 1600−1640 cm^{-1}, but they were masked by the intense isocyanurate absorption. Other important absorptions at lower energies than the carbonyl include a band at 1530 cm^{-1} that is assigned to N−H bending coupled to C−N stretching,[31] and the bands at 1244, 1120, and 1048 cm^{-1} attributed to the tri-ethylene glycol and urethane asymmetric and symmetric C−O−C stretches.[31,32] The methylene ($-CH_2-$) in-plane bending was observed at 764 cm^{-1}.[33] At higher energies than the carbonyl, all C−H stretches appeared at lower energies than 3000 cm^{-1} as two bands at 2900 and 2850 cm^{-1} consistent with their aliphatic character. The N−H stretch was broad extending the region from 3100 to 3800 cm^{-1} and could be deconvoluted using the Origin 8.7 software package as described previously[13,14] into a band assigned to a free N−H stretch in the 3423−3545 cm^{-1} range, into a second band assigned to the N−H stretch of NH H-bonded to carbonyl (NH···O=C) in the 3331−3341 cm^{-1} range, and a third, lower intensity band assigned to the N−H stretch of NH H-bonded to glycol groups ($NH\cdots O(CH_2)_2$) in the 3204−3234 cm^{-1} range.[34] The relative intensities of the deconvoluted bands were about 3.0-to-7.0-to-0.2 for all materials, suggesting no significant differences in the chemical environment around the urethane NH groups among the different metal-salt catalyzed PIR−PUR aerogels. The ATR−FTIR spectra of some samples were also obtained after thermomechanical cycling (see below), and the ratio of the three bands was in general modified in slight favor of the NH···O=C hydrogen-bonded groups at the expense of the free N−H stretch.[35]

Similarly, the solid-state ^{13}C NMR spectra of the various samples were practically identical irrespective of the catalyst (Figure 3B). The resonances in the 15−45 ppm range were assigned to the CH_2 carbons coming from the triisocyanate. The resonances in the 60−80 ppm range correspond to the CH_2 carbons from TEG. A sharp resonance at approximately 149 ppm (marked as "d" in Figure 3B) was due to the carbonyl carbon of the isocyanurate ring of the triisocyanate. The resonance at 156 ppm (marked as "l" in Figure 3B) corresponds to the carbonyl carbon of the urethane groups. The d/l intensity ratios were similar in all materials obtained with the various catalysts (see Figure 3B).

Since the reactivity of the various catalysts varied widely (Figure 1C), the spectra of Figure 3 represent materials across the domain of the gelation time, and the fact that they were practically identical to one another signifies that the chemical composition did not depend on the gelation time. Reviewers, however, noted that the presence of a parallel isocyanate trimerization reaction that produces additional isocyanurate rings to those brought in by N3300A could not be ruled out by the spectroscopic data alone. Since this possibility could have important implications in the interpretation of the data along our stiffness−morphology hypothesis, it deserved attention. Unlike in this study, the PIR part of PIR−PURs is usually formed in situ by using an excess of NCO groups over OH and oftentimes is assisted by elevated temperatures.[36−39] When the trimerization reaction is catalyzed by metal ions, those typically enter the reaction scheme in specific coordination configurations (complexes).[40,41] None of these conditions were present here. Nevertheless, this possibility was tested experimentally via CHN elemental analysis of two samples from each catalyst, one obtained with a high- and one obtained with a low-catalyst concentration (all CHN analysis data are summarized in Table S2a of Appendix II in the Supporting Information). It was found that the low-catalyst samples consisted of C, 53.29 ± 1.46%; H, 7.49 ± 0.090%; N, 11.32 ± 0.095%; and O (by difference from 100%), 27.91 ± 1.72%. Similarly, the high-catalyst samples consisted of C, 53.24 ± 1.01%; H, 7.45 ± 0.062%; N, 11.27 ± 0.051%; and O (by difference from 100%), 28.04 ± 1.33%. There was no statistically significant difference (via Student's *t*-test—assuming either equal or unequal variances) between the two sets of values for each element. Furthermore, these values were close to the theoretical composition of the polyurethane expected by mixing N3300A and TEG at the required

https://doi.org/10.1021/acsapm.3c00882
ACS Appl. Polym. Mater. 2023, 5, 6851−6863

stoichiometric ratio (=2:3) for complete reaction to polyurethane: C, 54.32%; H, 7.81%; N, 11.52%; and O, 26.34%. (Note that pure polyisocyanurate from Desmodur N3300A would consist of C, 57.14%; H, 7.14%; N, 16.67%; and O, 19.05%.) Based on these results, diversion of N3300A toward polyisocyanurate (PIR) was deemed highly unlikely under our experimental conditions, thereby all materials of this study share the common chemical composition illustrated in Scheme 1.

Albeit being chemically similar and having been formulated at the same 20% w/w concentration of monomers in the sol, the PIR–PUR aerogels of this study did show some small variations in their basic material properties (see Table S2b of Appendix II in the Supporting Information). Samples shrunk linearly relative to the dimensions of their molds, typically in the 20–30% range. Within each catalyst, in some cases, the trend was that as the catalyst concentration decreased, that is, at longer gelation times, shrinkage also decreased (e.g., $AlCl_3$ and Cu_2Cl_2). In other cases, as the catalyst concentration decreased, shrinkage first decreased, then increased, and then decreased again (e.g., $CoCl_2$ and $FeCl_3$). In yet other cases, shrinkage varied randomly (case of $CuCl_2$). Higher shrinkages lead to higher bulk densities, which, however, were all mostly in the range of 0.3–0.4 g cm^{-3} for all catalysts and all concentrations. Unlike other PIR–PUR aerogels in which the PIR functionality was prepared in situ by using a stoichiometric excess of isocyanate, and where oftentimes the catalyst concentration defined a directional path for the shrinkage and the bulk density,[36,37] the density variation over all samples of this study followed a random pattern just like shrinkage. The skeletal densities (ρ_s) of all the PIR–PUR aerogels were between 1.203 and 1.240 g cm^{-3}, and the porosities (Π) calculated from the bulk and skeletal density data via $\Pi = 100 \times (\rho_s - \rho_b)/\rho_s$ were in the range of 69–75% v/v. BET surface areas were about 1 m^2 g^{-1} or less (Table S2b), consistent with a lack of any fine nanostructure inside the micron-sided skeletal features visible in SEM (see the next section).[42]

2.3. Micromorphology of PIR–PUR Aerogels and Its Relationship to Thermal Conductivity as a Proxy to other Bulk Material Properties. Representative microstructures are shown in Figure 4. Throughout the sample range, the smallest features were in the micron-size regime. However, one consistent theme was that at short gelation times (around 5 min or less), which could be achieved either with very active catalysts (Figure 1C) or with high concentrations of even the less active ones (e.g., Figure 1B), the microstructures were bicontinuous, meaning that the solid and the pore networks looked similar, and in fact, they could be conceptually interchanged. Interestingly, particles could still be discerned on bicontinuous frameworks, but now the diameters of the interparticle connecting necks were approximately equal to the diameters of the particles themselves. As the gelation time increased (to 20–30 min or so), the network consisted of small microspheres interconnected with necks narrower than their diameters. Eventually, at long gelation times (75 min or more), achievable either with about the standard (1×) concentration of the less active catalysts of Figure 1C or with low concentrations of the more active catalysts (Figure 1B), smaller spheres seem to have coalesced into larger spherical particles. Polyurethane formation (Scheme 1) is a well-defined step-growth process that goes from oligomers to polymers.[30,44] The microstructural evolution as a function of the gelation time adds another

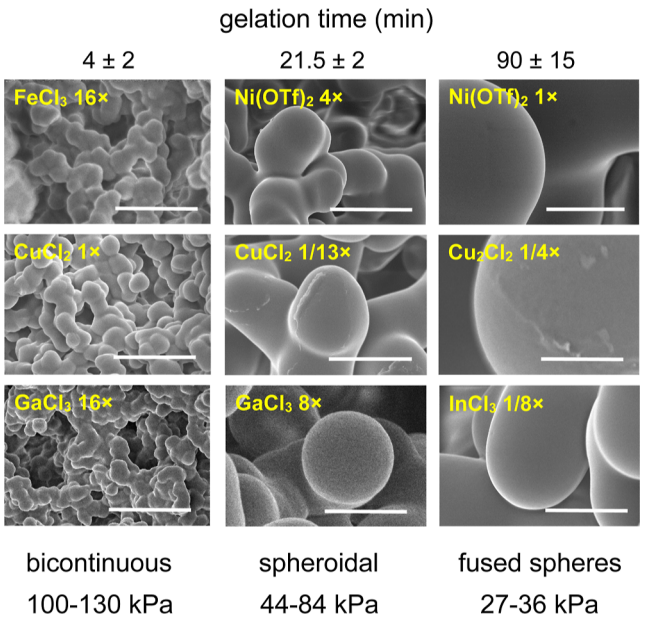

Figure 4. Scanning electron microscopy (SEM) of representative samples across the domain of the catalysts and their concentrations. Images are segregated in columns according to the gelation time. Magnification: 10,000×. Scale bars: 5 μm.

element into that process as it bears the signature of an early separation of a liquid phase of oligomers;[23] within that phase, the metal-salt-catalyzed step-growth polymerization process continues until the phase gets solidified. Depending on the catalyst and its concentration, solidification may happen fast, freezing (chemically) the network into a bicontinuous morphology, or slow, allowing time for coalescence of the liquid phase of oligomers into small droplets that coalesce further into larger ones if the reaction (solidification) time is even slower.[12,23] The overarching conclusion at this point is that the use of different catalysts has allowed control over the morphology of this class of aliphatic polyurethane gels and leaves little room for doubt that the major if not the only factor that controls nanomorphology is the gelation time.

Extracting particle diameters from SEM data for small and large spherical particles was straightforward. However, since particles were still discernible on bicontinuous frameworks (see for example, the "4 ± 2" column in Figure 4), using the ImageJ software package,[45] every concave curve along bicontinuous frameworks could be fitted to a circle whose diameter was associated with the diameter of a particle, albeit fused with its neighbors as described above. Choosing aerogels produced with $CuCl_2$ as an example, Figure 5A shows a strong correlation of particle diameters with the corresponding gelation times. Subsequently, because all samples of this study were made with the same amount of material (recall that the monomer concentration was fixed at 20% w/w throughout this study), it was reasoned that fewer but large well-separated spheres leave the least amount of material in the interparticle neck zones, while at the opposite end, small, merged skeletal particles with neck diameters close to the particle diameters place the maximum amount of material in the neck zones. If this hypothesis is correct, properties like the solid thermal conduction, λ_s, are expected to be higher through bicontinuous materials obtained at short gelation times. Figure 5B,C shows the total thermal conductivity (λ_{Total} – primary data) and the through-the-solid thermal conductivity (λ_s) of the various

https://doi.org/10.1021/acsapm.3c00882
ACS Appl. Polym. Mater. 2023, 5, 6851–6863

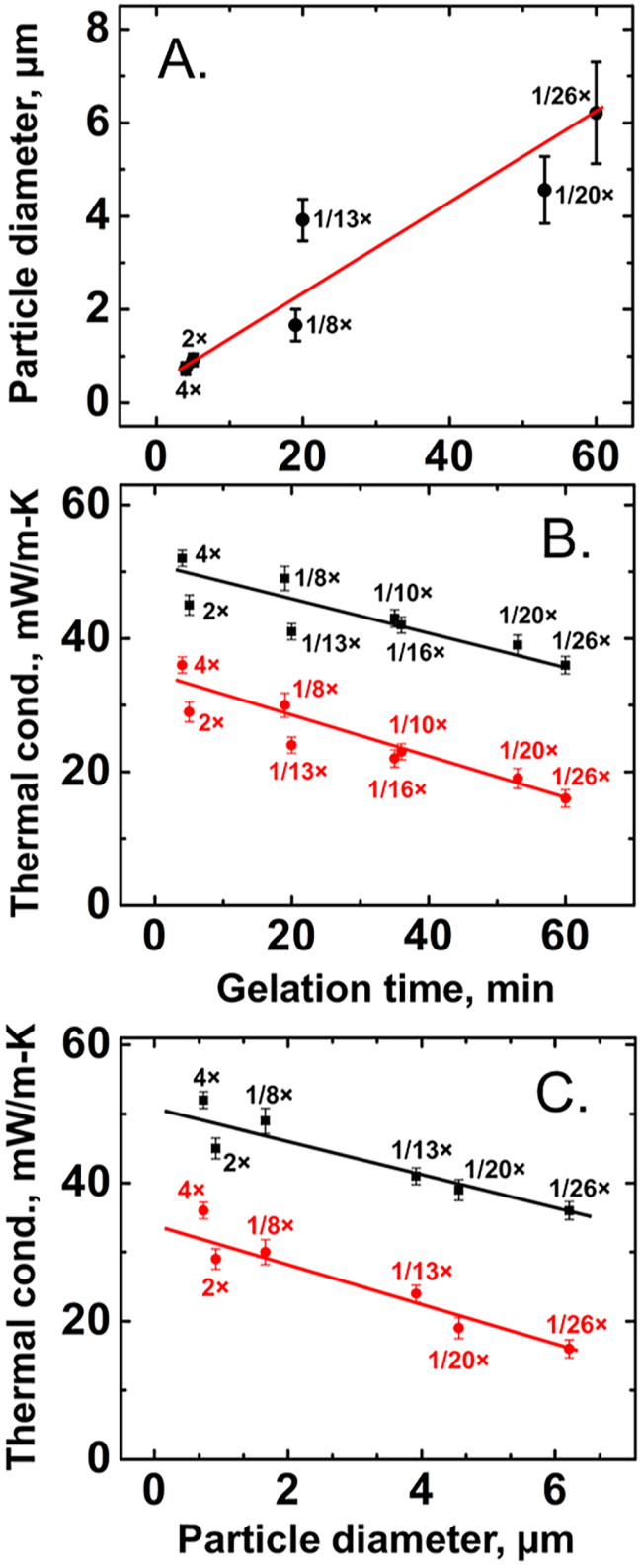

Figure 5. (A) Correlation of particle diameters calculated from SEM images via the ImageJ software,[45] and phenomenological gelation times of $CuCl_2$-catalyzed PIR−PUR aerogels at the concentrations shown (R^2 = 0.83). (B) Total thermal conductivity (λ_{Total}, black line, R^2 = 0.66) and through-the-solid thermal conductivity (λ_s, red line, R^2 = 0.83) of $CuCl_2$-catalyzed samples as a function of the gelation time. (C) Total thermal conductivity (λ_{Total}, black line, R^2 = 0.82) and through-the-solid thermal conductivity (λ_s, red line, R^2 = 0.89) of $CuCl_2$-catalyzed samples as a function of the particle diameter.

$CuCl_2$-derived aerogels as functions of either the gelation time or the diameters of the skeletal particles.

The λ_{Total} data of Figure 5 were obtained using the hot plate method as described in the Experimental Section. A photograph of the thermal conductivity apparatus is shown in Figure S1 of Appendix III in the Supporting Information. The solid thermal conductivity was calculated via $\lambda_s = \lambda_{Total} - \lambda_g$. (All λ_{Total} data and the data needed for the calculation of the λ_g correction toward λ_s are summarized in Table S3 of Appendix III in the Supporting Information). Owing to the similar porosities and pore sizes of the various samples of this study, the correction for the gaseous thermal conductivity (λ_g) upon λ_{Total} was similar for all samples (near the thermal conductivity of the open still air), and therefore, both λ_{Total} and λ_s followed the same trend with both the gelation time and the particle diameter—only the correlation improved when considering λ_s (see the legend of Figure 5). Specifically, both λ_{Total} and λ_s exhibited inverse relationships with gelation time and the diameter of the skeletal particles; the highest thermal conductivity values were observed in the bicontinuous samples (Figure 5B,C). This is consistent with the fact that restrictions along a thermal conductor, for example, in the form of necks along the strings of spheres, comprise thermal resistors. The dependence of the thermal conductivity on the skeletal particle size of PIR−PUR aerogels in which the PIR part was formed in situ was discussed recently by Merillas et al.: in contrast to our findings, they observed an increase in particle size (from 25 to 82 nm) with increasing catalyst concentration.[38] The thermal conductivity of their structures reached its maximum at the maximum catalyst concentration, corresponding to their largest particles. The range of the particle size alone indicates a different gelation mechanism, most likely involving rapid phase separation of solid colloidal particles, forming a primary skeletal framework on which more polymer accumulated through further reactions of unreacted monomers and oligomers with surface functional groups. This type of apparent increase in particle size due to additional polymer accumulation on a primary skeletal framework has been reported before in conjunction with higher monomer concentration sols that gel fast.[4,11] Skeletal frameworks consisting of such merged particles due to post-gelation polymer accumulation resemble the bicontinuous morphology of this work, leading to the conclusion that bicontinuous and bicontinuous-like morphologies, no matter how they are reached, bottom-up or top-down, are better thermal conductors.

Further support for the role of the bicontinuous versus the spheroidal morphologies on macroscopic properties that depend on the interparticle neck zones is found through the mechanical characterization of the PIR−PUR aerogels of this study.

2.4. Mechanical Properties as a Function of the Morphology of the PIR−PUR Aerogels of This Study.

2.4.1. Thermomechanical Analysis and the Shape Memory Effect. The study of the mechanical properties of the PIR−PUR aerogels of this work was guided by the shape memory effect expected from this kind of materials[13−15] and was carried out using dynamic mechanical analysis (DMA) in the tension mode as a function of the temperature (see the Experimental Section). For this, first, it was investigated whether the glass-transition temperatures (T_g) were in line with what it was expected from this type of materials.[13−15] At temperatures lower than their T_g's, all samples displayed storage moduli (E') approximately 10× higher than their loss moduli (E''). T_g was

https://doi.org/10.1021/acsapm.3c00882
ACS Appl. Polym. Mater. 2023, 5, 6851−6863

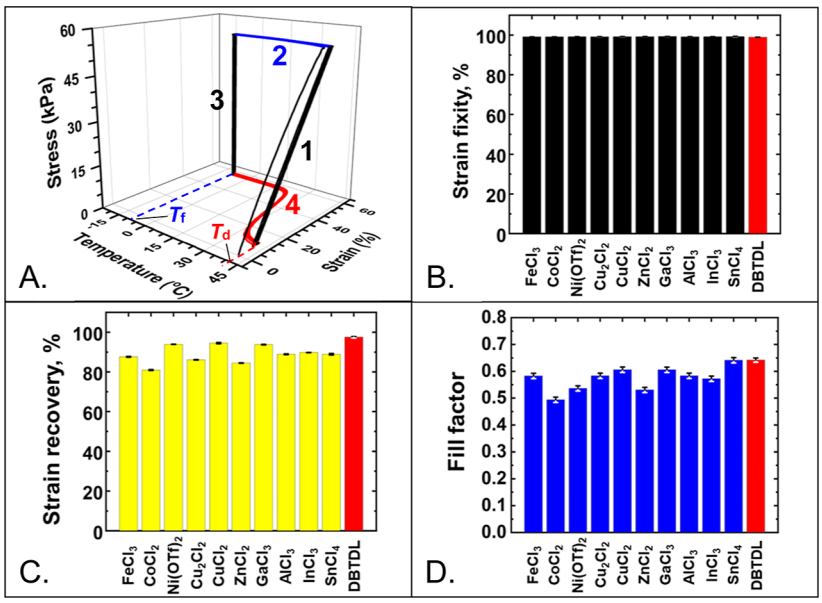

Figure 6. (A) Typical five-cycle thermomechanical experiment between deformation temperature (T_d) and fixing temperature (T_f—see text). (B–D) Average values of the three figures of merit (strain fixity, strain recovery, and fill factor) over cycles 2–5, for each catalyst over all their formulations and therefore gelation times and morphologies. (Note the negligible variability within each catalyst, but the non-insignificant variation across catalysts.)

defined as the temperature of the maximum value of the energy dissipation parameter, $\tan\delta = E''/E'$. The T_g values of all samples of this study were confined in a narrow range (30–34.5 °C) consistent with the fact that we are dealing with the same chemical composition throughout the materials domain of this study, as discussed in Section 2.2.

Once T_g had been determined, fresh, the as-prepared samples were heated to and equilibrated at their deformation temperature, $T_d = T_g + 10$ °C. Subsequently, they were stretched to near their break point (about 60% strain, determined previously with other samples), and the stress–strain curve was recorded (Figure 6A, segment 1). While under constant stress at their maximum elongation (strain), the samples were cooled to their fixation temperature, T_f (=T_g − 20 °C)—see Figure 6A, segment 2. At T_f, stress was removed (Figure 6A, segment 3), and the samples were allowed to equilibrate at T_f at the foot of segments 3 for 15 min. As noted in Figure 6A, segment 3, the samples retained most of the strain even though stress had been removed. Finally, the samples were heated back up to their recovery temperature (T_r = T_d = T_g + 10 °C—see Figure 6A, segment 4). Strain was recorded and is reported throughout all the four phases of the experiment of Figure 6A. In general, during this first thermomechanical cycle, strain recovery was not complete; a small amount of residual strain was retained within the samples due to molecular settling phenomena.[13−15] The stretch-cool/fix–recover cycle was repeated another four times. Post-settling, the stress–strain–temperature curves of Figure 6A practically coincided with one another, and the strain recovery after each cycle was complete.

The shape memory effect of the samples of this study is assessed via three figures of merit: the strain fixity and the strain recovery ratios and the fill factor. Of interest is also the elastic modulus. The figures of merit of all samples for all the five cycles are given in Tables S4–S6 of Appendix IV in the Supporting Information. Elastic moduli were obtained from the slopes of segment 1 of Figure 6A-type of data for every material and are provided in Table S7 of Appendix V in the Supporting Information.

Quantitatively, the strain fixity ratio, $R_f(N)$, quantifies how well a sample retains its temporary (stretched) shape at the foot of segment 3 of Figure 6A, that is, at temperatures sufficiently lower than T_g after stress is removed and samples are given time to equilibrate. $R_f(N)$ was calculated for each cycle, N, via eq 1

$$R_f(N) = \frac{\varepsilon_u(N)}{\varepsilon_m(N)} \times 100 \tag{1}$$

where $\varepsilon_u(N)$ is the equilibrium strain in the sample at the bottom of segment 3 of the curve of Figure 6A, and $\varepsilon_m(N)$ is the maximum strain imposed on a sample at T_d of each cycle. In general, for PIR–PUR shape memory aerogels, $R_f(N)$ is near 100%.[13−15] Indeed, the strain fixity ratio of all samples from all catalysts of this study was around 99% (Figure 6B).

The strain recovery ratio, $R_r(N)$, quantifies the ability of the samples to recover their initial dimensions (shape) after each thermomechanical cycle. $R_r(N)$ was calculated for each cycle, N, via eq 2

$$R_r(N) = \frac{\varepsilon_m(N) - \varepsilon_p(N)}{\varepsilon_m(N)} \times 100 \tag{2}$$

where $\varepsilon_p(N)$ is the residual strain at the end of segment 4 of the curve of Figure 6A. All $R_r(N)$ values of all the different samples of this study are summarized in bar graph form (Figure 6C) as averages of post-settling cycles 2–5 of all samples within each catalyst. Based on the small standard deviations, it was concluded that there was no significant variation in strain recovery among samples from various concentrations of the same catalyst; therefore, there was no significant variation in strain recovery as a function of the gelation time and morphology, but there was some variability between the various catalysts. The lowest average $R_r(N)$ value was noted for the samples prepared with $ZnCl_2$ (85%), and the

https://doi.org/10.1021/acsapm.3c00882
ACS Appl. Polym. Mater. 2023, 5, 6851–6863

highest $R_r(N)$ values were obtained with $GaCl_3$ (93%) and $CuCl_2$ (94%).

Finally, the fill factor, FF(N), the overall performance assessor for the shape memory effect, was calculated as the ratio of the area under the strain versus temperature curve over the projection of the entire 3D thermomechanical curves like those of Figure 6A on the temperature/strain plain. The FF(N) values depend on the recovery rate, namely, on the sharpness of the sigmoidal part of the recovery curve on the temperature/strain plain. Just like $R_r(N)$, there was no significant variation in the average FF(N) values for $2 \leq N \leq 5$ among samples from various concentrations of the same catalyst, which clearly includes samples with different morphologies, but there was variability between samples obtained with different catalysts. In addition, although the differences in the average post-settling values of R_r ($2 \leq N \leq 5$) and FF ($2 \leq N \leq 5$) among aerogels from different catalysts were small, nevertheless, they were not statistically insignificant. Since the variation pattern of R_r ($2 \leq N \leq 5$) was different from that of FF ($2 \leq N \leq 5$), the variation in the former cannot be the sole cause for the variation in the latter. Since FF ($2 \leq N \leq 5$) includes contributions of the rate of recovery and because the recovery here was driven by the imposed temperature ramp (1 °C min^{-1}), it is speculated that part of the variation in the FF ($2 \leq N \leq 5$) was due to non-equilibrium thermal conditions during shape recovery, which of course is affected by the thermal conductivity that changes with the morphology as discussed in Section 2.3 above. That variability of FF ($2 \leq N \leq 5$) among catalysts notwithstanding, for most samples, the average FF ($2 \leq N \leq 5$) values were over 0.55, which furnishes a robust shape memory effect.[13−15]

2.5. Stiffness and Morphology. As mentioned above, the elastic modulus, E, of the various PIR−PUR samples was determined from the slopes of the stress−strain curves at T_d (Figure 6A, segment 1), and all values for all samples are provided in Table S7 of Appendix V in the Supporting Information. The average E values of the post-settling moduli (cycles 2−5) decreased with increasing gelation time; that is, samples consisting of bicontinuous networks, coming from the shortest gelling sols, were stiffer than samples consisting of spheroidal networks from longer gelling sols, which in turn were stiffer than samples consisting of larger spheres from the longest gelling sols. For typical values of the elastic moduli together with the images of the corresponding morphologies, refer to Figure 4. Since the gelation time and the skeletal particle size are related (see, for example, Figure 5A), it follows that the elastic moduli should be related to the particle sizes. Indeed, as shown in Figure 7, all E values of all samples prepared with all catalysts at all concentrations are cumulatively related via an inverse exponential relationship to the skeletal particle diameters. If the E values get normalized for either tractable (e.g., small variations in bulk density), or intractable factors (reflected on small variations in fill factors), the scatter among experimental points noted in Figure 7 is reduced albeit by not much (see Figure S2 of Appendix V in the Supporting Information): the correlation coefficient increased from 0.59 in Figure 7 to 0.61 and 0.64, respectively, in Figure S2. The conclusion from Figures 7 and S2 is that the stiffness increases as the particle size decreases, the limit of course being when skeletal particles mostly merge to form a bicontinuous network.

Finally, as it was discussed previously,[46] and modeled recently both analytically and numerically by Ratke et al.,[47] the

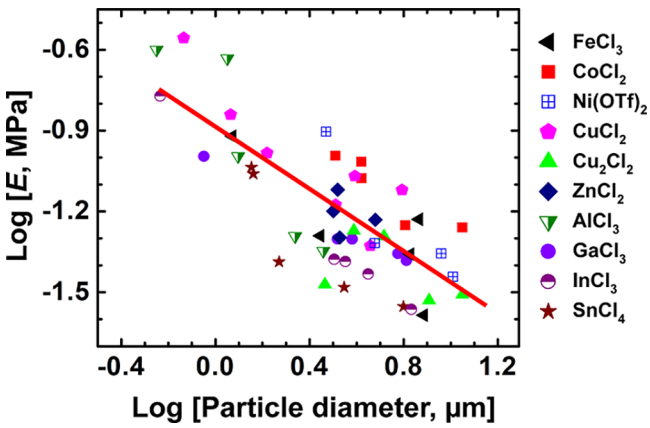

Figure 7. Double-logarithmic plot of the average (over cycles 2−5) elastic moduli, E, of all samples prepared with all catalysts at all concentrations vs the particle diameter of each sample. Correlation coefficient: 0.59. Particle diameters (from Table S2b) were calculated from the SEM data using the ImageJ software package.[45] (Refer also to Figure S2 of Appendix V in the Supporting Information).

stiffness of aerogels consisting of assemblies of interconnected spherical particles depends on the size of the interparticle necks, which act as stress concentrators. (The corollary, of course, is that an assembly of interconnected spheres cannot be stronger than its weakest points—the interparticle links.) As it was discussed in Section 2.3, since all samples were made with the same amount of material (constant monomer concentration at 20% w/w throughout), large, well-separated spheres leave the least amount of material in the interparticle neck zones, and the stiffness of those structures is expected,[47] and it was found low (Figure 7). At the opposite end, smaller, merging skeletal particles with neck diameters close to the particle diameters can be thought of as coming from larger spheres by transferring material to the neck zones. These structures comprise the bicontinuous morphology, and their stiffness is high. To confirm the relationship of E with the size of interparticle necks, the average interparticle neck diameters, d_{neck}, were calculated from the SEM images using ImageJ,[45] just like it was done with the particle diameters, $d_{particle}$. The neck diameter values are included in Table S7 of Appendix V in the Supporting Information. As it was noted in Section 2.3, the $d_{particle}-d_{neck}$ difference was small (<10%) relative to $d_{particle}$ for bicontinuous morphologies and increased to 60% in aerogels consisting of large spheres. Equations 3 and 4 express the neck area ($\pi(d_{neck})^2/4$) within

$$\text{Neck area per unit aerogel volume} = b\frac{2}{3} \times \frac{\rho_b}{\rho_s} \times \frac{d_{neck}^2}{d_{particle}^3} \quad (3)$$

$$\text{Neck area per unit aerogel mass} = b\frac{2}{3} \times \frac{1}{\rho_s} \times \frac{d_{neck}^2}{d_{particle}^3} \quad (4)$$

the unit aerogel volume or the unit aerogel mass, respectively, of any aerogel. Coefficient "b" is the number of interparticle contacts per skeletal particle and is related to the overall connectivity of the network and therefore its mass fractal dimension.[4,48,49] Figure 8 shows a linear relationship between E and the neck area per unit aerogel mass according to eq 4, assuming for simplicity b = 1. This relationship supports both the model of bicontinuous frameworks as strings of mostly

https://doi.org/10.1021/acsapm.3c00882
ACS Appl. Polym. Mater. 2023, 5, 6851−6863

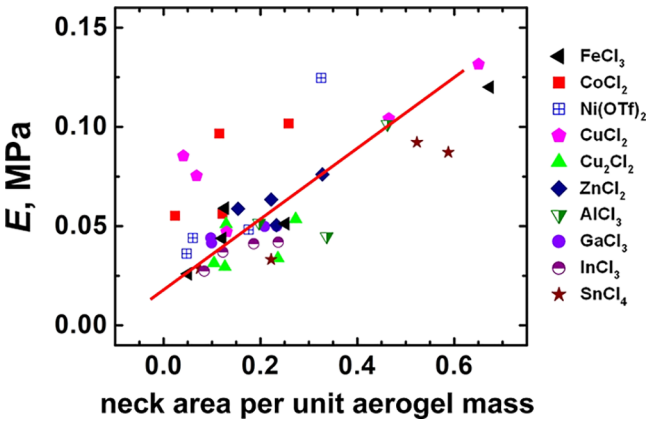

Figure 8. Average (over cycles 2−5) elastic moduli, E, of all samples prepared with all catalysts at all concentrations vs the neck area per unit aerogel mass (calculated via eq 4 assuming $b = 1$). Correlation coefficient: 0.77. Units of the horizontal axis: $cm^3\ g^{-1}\ \mu m^{-1}$.

merged spheres and the fact that the stiffness of aerogels consisting of interconnected spherical particles depends on the interparticle neck zone area, as predicted.[46,47]

3. CONCLUSIONS

Using aliphatic PIR−PUR aerogels as a model system, catalysis was used as a tool to control morphology. The catalytic activity of various metal salts, mostly chlorides, was linked to the skeletal morphology of the aerogels through the gelation time. All other parameters remaining constant (sol concentration, solvent), more active catalysts or higher concentrations of the less active ones brought about fast gelation, and the corresponding gels had a bicontinuous morphology. As the gelation time increased, bicontinuous structures underwent spherulization first into smaller and then larger microspheres. This sequence is consistent with early phase separation of oligomers as an oily liquid phase that gets solidified later as polymerization progresses. Having deconvoluted micromorphology from other material properties like density and porosity, it was possible to show experimentally that the elastic modulus and the thermal conduction through the solid were related to the network morphology: bicontinuous structures were stiffer and better thermal conductors than structures consisting of small and then of larger microspheres. This was attributed to the size of the interparticle neck zones, which in the bicontinuous morphologies are almost as wide as the diameters of the skeletal particles.

4. EXPERIMENTAL SECTION

4.1. Sourcing of Materials. All reagents and solvents were used as received unless noted otherwise. The aliphatic triisocyanate is available as a pure chemical under the trade name Desmodur N3300A and was donated generously by Covestro LLC (Pittsburg, PA). TEG, DBTDL, anhydrous cupric chloride ($CuCl_2$), cuprous chloride (Cu_2Cl_2), ferric chloride ($FeCl_3$), zinc chloride ($ZnCl_2$), aluminum chloride ($AlCl_3$), nickel triflate ($Ni(OTf)_2$), cobalt chloride ($CoCl_2$), tin chloride ($SnCl_4$), gallium chloride ($GaCl_3$), indium chloride ($InCl_3$), thallium nitrate ($Tl(NO_3)_3$), bismuth chloride ($BiCl_3$), cadmium nitrate ($Cd(NO_3)_2$), and anhydrous acetonitrile were purchased from Sigma-Aldrich. Deuterated acetonitrile (CD_3CN) (99.5% atom D) were purchased from Cambridge Isotope Laboratories, Inc. (Tewksbury, MA). Siphon-grade CO_2, N_2 (99.999%), and CO_2 (99.999%) were purchased from Air Gas Co (St. Louis, MO).

4.2. Sol Formulation and Preparation of Shape Memory PIR−PUR Aerogels. The synthesis of the PIR−PUR aerogels of this study was carried out at room temperature in anhydrous acetonitrile. The triisocyanate (Desmodur N3300A) to diol (triethylene glycol, TEG) ratio was set equal to 2:3 mol/mol, and the total weight percent of the two monomers in the sol remained constant at 20% w/w throughout. The only variable among the various sol formulations was the chemical identity of the catalyst and its concentration. All catalyst concentrations are referred to as multiples (e.g., 1×, 2×, 1/2×, and 1/4×) of a reference concentration (designated as 1×), which was the concentration of DBTDL used in our previous studies of the shape memory properties of a similar type of PIR−PUR aerogels.[13−15] To set that standard concentration, the amount of DBTDL had been set equal to the 1/120 mol/mol of Desmodur N3300A, and in turn that amount had been decided based on the fact it gave reasonable gelation times; for example, at 20% w/w sol concentration, the gelation time was about 30 min. Thus, in a typical gelation using the standard (or 1×) concentration of DBTDL as a catalyst, 2.520 g (5.00 mmol) of Desmodur N3300A was weighed in a vial, and 8.55 mL of acetonitrile was added. Meanwhile, 1.125 g (7.50 mmol) of TEG was weighed in a 50 mL round-bottom flask, and 10 mL of anhydrous acetonitrile was added. As soon as TEG was dissolved, 25.0 μL (0.0266 g, 0.0422 mmol) of neat DBTDL was added directly into the TEG solution. A few seconds later, after DBTDL had been dissolved, the isocyanate solution was added, using a syringe, to the round-bottom flask containing the solution of TEG and DBTDL; the mixture was stirred for about a minute, and then it was poured in plastic syringes (Plastic Norm-Ject Syringes, 20 mL, Fisher Scientific Catalogue no. 14-817-32, 2.53 cm inner diameter) used as molds.

This procedure was adapted to most of the anhydrous metal salts used as catalysts in this study. For this, stock solutions of the metal salts were prepared in a glove box using anhydrous acetonitrile as a solvent and at concentrations that depend on their catalytic activity. All sol formulations with all salts at all concentrations are presented in Table S1 of Appendix I in the Supporting Information. The volume of the stock solution that was transferred for each sol was subtracted from the volume of acetonitrile used to dissolve the triisocyanate and the diol, so that the total volume of the sol and thereby the total monomer concentration in the sol would remain constant. For example, for making a $CuCl_2$ stock solution, anhydrous $CuCl_2$ (2.789 g, 0.0207 mol) was weighed inside a glove box and was dissolved in 250 mL of acetonitrile in a volumetric flask ($[CuCl_2]_{in\_stock\_solution}$ = 0.0828 M). In order to prepare a sol with about the same concentration of the catalyst as in the standard DBTDL sol above, referred to as $CuCl_2$-1× sol, we used 500 μL of this $CuCl_2$ stock solution (containing 0.0414 mmol of $CuCl_2$). Thus, for making that sol, Desmodur N3300A (2.520 g, 5.00 mmol), was weighed in a vial and was dissolved with 8.55 mL of anhydrous acetonitrile; meanwhile, TEG (1.125 g, 7.50 mmol) was weighed directly in a 50 mL three-neck round-bottom flask and was dissolved under N_2 with 9.50 mL of anhydrous acetonitrile at 23 °C. The 500 μL of the stock $CuCl_2$ solution was added to the TEG solution, the mixture was stirred for 1 min, followed by addition of the isocyanate solution. The resulting sol was stirred for another minute and was poured into plastic syringes used as molds (see above). The molds were covered with a parafilm and were stored at room temperature for gelation and aging. The gelation time varied from about 1 min to around 24 h depending on the metal catalyst and its concentration. All gelation times along with other material properties of the resulting aerogels are presented in Table S2b of Appendix II in the Supporting Information. The aging time was kept at about 16 h for all samples. This procedure was repeated several times by varying only the volume of the $CuCl_2$ stock solution that was mixed with the TEG solution, which in turn was always made with 10 mL of anhydrous acetonitrile minus the volume of the $CuCl_2$ stock catalyst solution that was transferred into it, so that the total volume of the TEG/catalyst solution was always equal to 10 mL. As it was mentioned above, the resulting sols are referred to as 4×, 2×, 1×, 1/2×, 1/4×, and so forth depending on the concentration of the catalyst with respect to the concentration of DBTDL used in the reference sol as described above. Stock solutions of $SnCl_4$,

https://doi.org/10.1021/acsapm.3c00882
ACS Appl. Polym. Mater. 2023, 5, 6851−6863

$Tl(NO_3)_3$, Cu_2Cl_2, $CoCl_2$, $InCl_3$, $AlCl_3$, $Ni(OTf)_2$, $ZnCl_2$, $FeCl_3$, and $GaCl_3$ were prepared in a similar manner as just described for $CuCl_2$ (see Table S1 of Appendix I in the Supporting Information). Sometimes, sonication of the volumetric flask after it was taken out of the glove box helped in the dissolution. The cases of $BiCl_3$ and $Cd(NO_3)_2$ were somewhat different. Those two salts were sparingly soluble in pure anhydrous acetonitrile, but the solubility improved dramatically in the presence of TEG. Thus, with these two salts, only the 1× formulation was attempted by weighing and adding the correct amounts of the solid salts in the TEG solution, following closely the procedure used with DBTDL.

After aging, wet gels were removed from the molds, washed first with acetonitrile twice, and then with acetone six times. Each wash lasted for 8 h, and the volume of the solvent used was 4× the volume of each wet gel. Finally, acetone-exchanged wet gels were dried with SCF CO_2 as described in the next section. The resulting aerogels are referred to according to the metal salt used as the catalyst and its relative concentration (2×, 1×, 1/2×, 1/4×, etc.), just like the corresponding sols.

4.3. Methods. *4.3.1. Gelation Process.* The rheological behavior of several sols was monitored during gelation with a TA Instruments AR 2000ex Rheometer using a cone (60 mm diameter, 2° angle) and a Peltier plate geometry with a 500 μm gap between them. The instrument was operated in the oscillation mode, and time sweep experiments were performed with a fixed-strain amplitude from the moment of adding the Desmodur N3300A solution into the TEG/catalyst solution. The gel point was determined using a dynamic multiwave method with five superimposed harmonics with frequencies 1, 2, 4, 8, and 16 rad s^{-1}. The strain of the fundamental oscillation (1 rad s^{-1}) was set at 5%.

4.3.2. Drying. Drying of wet gels was carried out in an autoclave (SPIDRY Jumbo Supercritical Point Dryer, SPI Supplies, Inc. West Chester, PA, or a Spe-edSFE system, Applied Separations, Allentown, PA). Samples were loaded into the autoclave at room temperature submerged in fresh acetone filling the sample boat. The pressure vessel was closed, and liquid CO_2 was allowed in at room temperature. Acetone was drained out from the pressure vessel while more liquid CO_2 was allowed in. Samples were kept under liquid CO_2 for 30 min under 80−90 bar pressure at 14 °C. Then, liquid CO_2 was drained out while more liquid CO_2 was allowed in the vessel. The 30 min stay/drain cycle was repeated several times until all acetone was extracted from the pores of the samples; at that point, CO_2 coming out from drain formed a stream of dry ice. Subsequently, the temperature of the autoclave was raised to 40 °C (well above the critical temperature of CO_2), and that condition was maintained for 1 h. Finally, the SCF CO_2 was vented off the autoclave slowly, behaving like a gas.

4.3.3. Chemical Characterization. CHN elemental analysis was conducted at Galbraith Laboratories (Knoxville, TN 37921) using a combustion method. Data are summarized in Table S2a of Appendix II in the Supporting Information.

Attenuated total reflectance (ATR) FTIR spectroscopy was carried out with a Nicolet iS50 FT-IR, equipped with an ATR accessory model 0012-3XXT. The samples were cut to small chunks that were placed on the diamond crystal (2.8 mm in diameter, with a sampling zone of 2 mm), and ATR−FTIR spectra were obtained by pressing the samples against the crystal with the ATR unit's pressure device (gripper). The maximum throughput of the infrared beam to the detector was achieved via optical alignment that was performed with no sample on the crystal. Data were collected at an incident beam angle of 45° using 32 scans with a resolution of 2 cm^{-1}. In the ATR mode, the penetration depth (pd) and thereby the effective path length (=number of reflections × pd) of the infrared beam are directly proportional to the wavelength. Thus, an ATR correction was applied by the software of the instrument to the raw data by multiplying the spectra with a wavelength-dependent factor (roughly $\lambda/5$) that adjusted the relative peak intensities. The ν(N−H) bands of several randomly selected spectra were deconvoluted into three Gaussian-shaped peaks using the Origin 9.7 software package.

Liquid-phase ^{119}Sn NMR spectra were recorded with a 400 MHz Varian Unity Inova NMR instrument (^{119}Sn frequency of 149 MHz). Liquid-phase ^{119}Sn NMR spectra were referenced externally using a coaxial tube to tetramethyltin (0 ppm). Solid-state CP TOSS ^{13}C NMR spectra were obtained with a Bruker AVANCE III 400 MHz spectrometer (^{13}C frequency of 100 MHz), using a 7 mm Bruker MAS probe at a magic-angle spinning rate of 5 kHz, with broadband proton suppression. For this, the aerogel samples were cut in small chunks and were pressed in the rotor. The relaxation delay was set at 5 s. Solid-state ^{13}C NMR spectra were referenced externally to glycine (carbonyl carbon at 176.03 ppm). Chemical shifts are reported versus tetramethylsilane (0 ppm).

4.3.4. Physical Characterization. Bulk densities (ρ_b) were calculated from the weight and physical dimensions of the samples. Skeletal densities (ρ_s) were determined with helium pycnometry using a Micromeritics AccuPyc II 1340 instrument. Porosities (Π), as percent of empty space, were calculated from the ρ_b and ρ_s values via $\Pi = 100 \times [(\rho_s - \rho_b)/\rho_s]$. Samples were outgassed for 24 h, at 40 °C, under vacuum, before skeletal density determinations.

4.3.5. Structural Characterization. Structural characterization was carried out with SEM with Au/Pd (60/40)-coated samples on a Hitachi field-emission microscope model S-4700. The samples were placed on the stub using C-dot. Thin sticky copper strips were cut and placed on the edges and top of the sample, leaving a small area uncovered for observation.

4.3.6. Thermomechanical Characterization. Thermomechanical characterization was carried out in the tension mode with a TA Instruments Q800 Dynamic Mechanical Analyzer (DMA) equipped with a tension clamp (TA Instruments part no. 984016.901, load cell 18 N). All specimens for testing had a rectangular geometry (length 20 mm, width 15 mm, and thickness 4−5 mm) in the spirit of ASTM D790-10 and ASTM D4065. The samples were cut off with a knife from larger cylindrical samples dipped in liquid N_2 and were sanded with a 3 M sandpaper (320 grit, part no. 98401) while still at cryogenic temperature.

For the determination of glass-transition temperatures (T_g), specimens were placed in the load cell at room temperature, and a small tensile force (0.01 N) prevented them from bending. The temperature was stepped to the initial testing temperature, and samples were equilibrated at that temperature for 5 min. Glass-transition temperatures (T_g) were extracted from the viscoelastic properties of the samples, which were measured by applying a continuous sinusoidal oscillation (1 Hz) with a strain amplitude equal to 0.3%, while the temperature was ramped from −150 to 150 °C at 3 °C min^{-1}. During this time, the loss and storage moduli (E'', and E', respectively) were recorded as functions of temperature. T_g was identified as the maximum of the tan δ ($=E''/E'$) plot as a function of temperature.

The shape memory behavior was studied in the controlled force mode. Samples were fixed in the load cell at room temperature, and then they were equilibrated at their deformation temperature ($T_d = T_g$ + 10 °C) for 5 min. Subsequently, samples were stretched with a small tensile force (0.01 N); their length was measured by the instrument and was stored as the starting point. Next, specimens were stretched at a constant force rate of 1 N min^{-1} up to near their break point (typically around 60% strain, which was determined previously with an independent test and another sample), and then they were cooled at 5 °C min^{-1}, while under the final stress, to their fixation temperature ($T_f \ll T_g$, typically $T_f = T_g - 20$ °C). At that point (T_f), the samples were equilibrated for 5 min, and the tensile force was reduced to 0.01 N. The samples were allowed to relax (fix) under the new stress condition for 15 min (always at T_f), while strain was recorded continuously. Finally, the samples were heated at 1 °C min^{-1} to their recovery temperature ($T_r = T_d$) while strain was still recorded. The samples were held at T_d for 15 min, and the cycle was repeated. Five such cycles were run successively for each sample, and data were analyzed to extract the elastic moduli and the figures of merit of the shape memory effect (strain fixity, strain recovery, and fill factors) in each cycle. Fill factors (FF(N)) were obtained for each thermomechanical cycle (N) using the ImageJ software package[45]

https://doi.org/10.1021/acsapm.3c00882
ACS Appl. Polym. Mater. 2023, 5, 6851−6863

to calculate the ratio of the area underneath the temperature/strain curves over the area under the projection of the entire 3D thermomechanical curve onto the temperature/strain plane.[13,14]

4.3.7. Thermal Conductivity. The total thermal conductivities, λ_{Total}, of the $CuCl_2$-catalyzed PIR–PUR aerogels were measured using a custom-made heat flowmeter that includes in sequence from top to bottom:[14] a 10 cm × 10 cm hotplate (at 37.5 °C, bottom), the PIR–PUR aerogel sample, a NIST-calibrated reference sample,[50] and a cold surface (an ice–water bucket)—a photograph of this experimental setup is shown in Figure S1 of Appendix III in the Supporting Information. The PIR–PUR aerogel samples used in that configuration were cast as large panels (10 cm × 10 cm × 1 cm) by scaling up the formulations of Table S1 in the Supporting Information. Those panels were used to cover the 10 cm × 10 cm stage of the hotplate. Solid thermal conductivities, λ_s, were calculated via $\lambda_s = \lambda_{Total} - \lambda_g$, whereas gaseous thermal conductivities, λ_g, were calculated using the Knudsen equation,[51] and assuming negligible heat transfer by radiation ($\lambda_{irr} \approx 0$).

■ ASSOCIATED CONTENT

Supporting Information

The Supporting Information is available free of charge at https://pubs.acs.org/doi/10.1021/acsapm.3c00882.

Appendix I, formulations of all PIR–PUR aerogels with all catalysts and catalyst concentrations; Appendix II, elemental analysis data, general material properties, and gelation times of all PIR–PUR aerogels; Appendix III, thermal conductivity apparatus and data of selected $CuCl_2$-catalyzed PIR–PUR aerogels; Appendix IV, figures of merit of the shape memory effect of the PIR– PUR aerogels; and Appendix V, elastic modulus data of all PIR–PUR aerogels with all catalysts and catalyst concentrations (PDF)

■ AUTHOR INFORMATION

Corresponding Authors

Nicholas Leventis − *Department of Chemistry, Missouri University of Science and Technology, Rolla, Missouri 65409, United States;* Present Address: Aspen Aerogels, 30 Forbes Road, Bldg. B, Northborough, MA 01532, United States; Phone: 508-847-1792; Email: nleventis@aerogel.com

Chariklia Sotiriou-Leventis − *Department of Chemistry, Missouri University of Science and Technology, Rolla, Missouri 65409, United States;* orcid.org/0000-0003-3283-8257; Phone: 573-341-4353; Email: cslevent@mst.edu

Authors

A. B. M. Shaheen ud Doulah − *Department of Chemistry, Missouri University of Science and Technology, Rolla, Missouri 65409, United States;* orcid.org/0000-0002-5413-0762

Chandana Mandal − *Department of Chemistry, Missouri University of Science and Technology, Rolla, Missouri 65409, United States*

Hojat Majedi Far − *Department of Chemistry, Missouri University of Science and Technology, Rolla, Missouri 65409, United States*

Vaibhav A. Edlabadkar − *Department of Chemistry, Missouri University of Science and Technology, Rolla, Missouri 65409, United States;* orcid.org/0000-0001-5763-7318

Rushi U. Soni − *Department of Chemistry, Missouri University of Science and Technology, Rolla, Missouri 65409, United States;* orcid.org/0000-0002-1855-8905

Stephen Y. Owusu − *Department of Chemistry, Missouri University of Science and Technology, Rolla, Missouri 65409, United States;* orcid.org/0000-0002-5251-4287

Complete contact information is available at: https://pubs.acs.org/10.1021/acsapm.3c00882

Notes

The authors declare no competing financial interest.

■ ACKNOWLEDGMENTS

We thank the NSF for the financial support under award number CMMI-1530603 (sub-contract to MS&T from Tufts University).

■ REFERENCES

(1) Leventis, N.; Sotiriou-Leventis, C.; Chandrasekaran, N.; Mulik, S.; Chidambareswarapattar, C.; Sadekar, A.; Mohite, D.; Mahadik, S. S.; Larimore, Z. J.; Lu, H.; Churu, G.; et al. Isocyanate-derived Organic Aerogels: Polyureas, Polyimides, Polyamides. *MRS Online Proc. Libr.* **2011**, *1306*, 301.

(2) Leventis, N.; Sotiriou-Leventis, C.; Zhang, G.; Rawashdeh, A.-M. M. Nano Engineering Strong Silica Aerogels. *Nano Lett.* **2002**, *2*, 957–960.

(3) Lee, J. K.; Gould, G. L.; Rhine, W. Polyurea based aerogel for a high performance thermal insulation material. *J. Sol-Gel Sci. Technol.* **2009**, *49*, 209–220.

(4) Chidambareswarapattar, C.; McCarver, P. M.; Luo, H.; Lu, H.; Sotiriou-Leventis, C.; Leventis, N. Fractal Multiscale Nanoporous Polyurethanes: Flexible to Extremely Rigid Aerogels from Multifunctional Small Molecules. *Chem. Mater.* **2013**, *25*, 3205–3224.

(5) Chidambareswarapattar, C.; Larimore, Z.; Sotiriou-Leventis, C.; Mang, J. T.; Leventis, N. One-step Room-temperature Synthesis of Fibrous Polyimide Aerogels from Anhydrides and Isocyanates and Conversion to Isomorphic Carbons. *J. Mater. Chem.* **2010**, *20*, 9666–9678.

(6) Leventis, N.; Chidambareswarapattar, C.; Mohite, D. P.; Larimore, Z. J.; Lu, H.; Sotiriou-Leventis, C. Multifunctional Porous Aramids (Aerogels) by Efficient Reaction of Carboxylic Acids and Isocyanates. *J. Mater. Chem.* **2011**, *21*, 11981–11986.

(7) Leventis, N. Three-Dimensional Core-Shell Superstructures: Mechanically Strong Aerogels. *Acc. Chem. Res.* **2007**, *38*, 874–884.

(8) Odian, G. *Principle of Polymerization*; Wiley-Interscience: New York, NY, 2004; p 130.

(9) Weigold, L.; Mohite, D. P.; Mahadik-Khanolkar, S.; Leventis, N.; Reichenauer, G. Correlation of Microstructure and Thermal Conductivity in Nanoporous Solids: The Case of Polyurea Aerogels Synthesized from an Aliphatic Tri-isocyanate and Water. *J. Non-Cryst. Solids* **2013**, *368*, 105–111.

(10) Leventis, N.; Chidambareswarapattar, C.; Bang, A.; Sotiriou-Leventis, C. Cocoon-in-web-like Superhydrophobic Aerogels from Hydrophilic Polyurea and Use in Environmental Remediation. *ACS Appl. Mater. Interfaces* **2014**, *6*, 6872–6882.

(11) Taghvaee, T.; Donthula, S.; Rewatkar, P. M.; Majedi Far, H.; Sotiriou-Leventis, C.; Leventis, N. K.-I. K-Index: A Descriptor, Predictor, and Correlator of Complex Nanomorphology to Other Material Properties. *ACS Nano* **2019**, *13*, 3677–3690.

(12) Leventis, N. Polyurea Aerogels: Synthesis, Material Properties, and Applications. *Polymers* **2022**, *14*, 969.

(13) Donthula, S.; Mandal, C.; Leventis, T.; Schisler, J.; Saeed, A. M.; Sotiriou-Leventis, C.; Leventis, N. Shape Memory Superelastic Poly(isocyanurate-urethane) Aerogels (PIR-PUR) for Deployable Panels and Biomimetic Applications. *Chem. Mater.* **2017**, *29*, 4461–4477.

(14) Donthula, S.; Mandal, C.; Schisler, J.; Leventis, T.; Meador, M. A. B.; Sotiriou-Leventis, C.; Leventis, N. Nanostructure-Dependent Marcus-Type Correlation of the Shape Recovery Rate and the

Young's Modulus in Shape Memory Polymer Aerogels. *ACS Appl. Mater. Interfaces* **2018**, *10*, 23321−23334.
(15) Malakooti, S.; ud Doulah, A. B. M. S.; Ren, Y.; Kulkarni, V. N.; Soni, R. U.; Edlabadkar, V. A.; Zhang, R.; Vivod, S. L.; Sotiriou-Leventis, C.; Leventis, N.; Lu, H. Meta-Aerogels: Auxetic Shape-Memory Polyurethane Aerogels. *ACS Appl. Polym. Mater.* **2021**, *3*, 5727−5738.
(16) Liu, C.; Qin, H.; Mather, P. T. Review of Progress in Shape-memory Polymers. *J. Mater. Chem.* **2007**, *17*, 1543−1558.
(17) Zhuo, H. T.; Hu, J. L.; Chen, S. J. Electrospun Polyurethane Nanofibres Having Shape Memory Effect. *Mater. Lett.* **2008**, *62*, 2074−2076.
(18) Lendlein, A.; Gould, O. E. C. Reprogrammable Recovery and Actuation Behaviour of Shape-Memory Polymers. *Nat. Rev. Mater.* **2019**, *4*, 116−133.
(19) Ashby, M. F. The Properties of Foams and Lattices. *Philos. Trans. R. Soc., A* **2006**, *364*, 15−30.
(20) de Lima, V.; da Silva Pelissoli, N.; Dullius, J.; Ligabue, R.; Einloft, S. Kinetic Study of Polyurethane Synthesis Using Different Catalytic Systems of Fe, Cu, Sn, and Cr. *J. Appl. Polym. Sci.* **2010**, *115*, 1797−1802.
(21) Schellekens, Y.; Van Trimpont, B.; Goelen, P. J.; Binnemans, K.; Smet, M.; Persoons, M. A.; De Vos, D. Tin-free Catalysts for the Production of Aliphatic Thermoplastic Polyurethanes. *Green Chem.* **2014**, *16*, 4401−4407.
(22) Robins, J. Structural Effects in Metal Ion Catalysis of Isocyanate-Hydroxyl Reactions. *J. Appl. Polym. Sci.* **1965**, *9*, 821−838.
(23) Nakanishi, K.; Tanaka, N. Sol-Gel with Phase Separation Hierarchically Porous Materials Optimized for High-Performance Liquid Chromatography Separations. *Acc. Chem. Res.* **2007**, *40*, 863−873.
(24) Leventis, N.; Elder, I. A.; Rolison, D. R.; Anderson, M. L.; Merzbacher, C. I. Durable Modification of Silica Aerogel Monoliths with Fluorescent 2,7-Diazapyrenium Moieties − Sensing Oxygen near the Speed of Open-Air Diffusion. *Chem. Mater.* **1999**, *11*, 2837−2845.
(25) Winter, H. H. Can the Gel Point of a Cross-linking Polymer Be Detected by the G'-G″ Crossover? *Polym. Eng. Sci.* **1987**, *27*, 1698−1702.
(26) Kim, S.-Y.; Choi, D.-G.; Yang, S.-M. Rheological Analysis of the Gelation Behavior of tetraethylorthosilane/vinyltriethoxysilane Hybrid Solutions. *Korean J. Chem. Eng.* **2002**, *19*, 190−196.
(27) Muthukumar, M. Screening Effect on Viscoelasticity Near the Gel Point. *Macromolecules* **1989**, *22*, 4656−4658.
(28) Irving, H.; Williams, R. J. P. 637. The stability of transition-metal complexes. *J. Chem. Soc.* **1953**, 3192−3210.
(29) Fărcaşiu, D.; Leu, R.; Ream, P. J. The 1 : 1 and 2 : 1 Complexes of Diethyl Ether with Tin Tetrachloride and Their Stability, Studied by ^{119}Sn NMR Spectroscopy. *J. Chem. Soc., Perkin Trans. 2* **2001**, 427−431.
(30) Dodge, J. Polyurethanes and Polyureas. In *Synthetic Methods in Step-Growth Polymers*; Rogers, M. E., Long, T. E., Eds.; Wiley: New York, NY, USA, 2003; pp 197−263.
(31) Silverstein, R. M.; Bassler, G. C.; Morrill, T. C. *Spectroscopic Identification of Organic Compounds*, 5th ed.; John Wiley & Sons, Inc.: New York, 1991; pp 32−33.
(32) McCarthy, S. J.; Meijs, G. F.; Mitchell, N.; Gunatillake, P. A.; Heath, G.; Brandwood, A.; Schindhelm, K. In-vivo Degradation of Polyurethanes: Transmission-FTIR Microscopic Characterization of Polyurethanes Sectioned by Cryomicrotomy. *Biomaterials* **1997**, *18*, 1387−1409.
(33) Defeyt, C.; Langenbacher, J.; Rivenc, R. Polyurethane coatings used in twentieth century outdoor painted sculptures. Part I: comparative study of various systems by means of ATR-FTIR spectroscopy. *Heritage Sci.* **2017**, *5*, 11.
(34) Mattia, J.; Painter, P. A Comparison of Hydrogen Bonding and Order in a Polyurethane and Poly(Urethane-Urea) and Their Blends with Poly(Ethylene Glycol). *Macromolecules* **2007**, *40*, 1546−1554.
(35) Teo, L. S.; Chen, C. Y.; Kuo, J. F. Fourier Transform Infrared Spectroscopy Study on Effects of Temperature on Hydrogen Bonding in Amine-Containing Polyurethanes and Poly(urethane−urea)s. *Macromolecules* **1997**, *30*, 1793−1799.
(36) Merillas, B.; Martin-de Leon, J.; Villafañe, F.; Rodriguez-Pérez, M. Á. Transparent Polyisocyanurate-polyurethane-based Aerogels: Key Aspects on the Synthesis and Their Porous Structures. *ACS Appl. Polym. Mater.* **2021**, *3*, 4607−4615.
(37) Diascorn, N.; Calas, S.; Sallée, H.; Achard, P.; Rigacci, A. Polyurethane aerogels synthesis for thermal insulation − textural, thermal and mechanical properties. *J. Supercrit. Fluids* **2015**, *106*, 76−84.
(38) Merillas, B.; Villafañe, F.; Rodríguez-Pérez, M. Á. Super-insulating Transparent Polyisocyanurate-polyurethane Aerogels: Analysis of Thermal Conductivity and Mechanical Properties. *Nanomaterials* **2022**, *12*, 2409.
(39) Zhu, Z.; Snellings, G. M.; Koebel, M. M.; Malfait, W. J. Superinsulating Polyisocyanate Based Aerogels: a Targeted Search for the Optimum Solvent System. *ACS Appl. Mater. Interfaces* **2017**, *9*, 18222−18230.
(40) Guo, Y.; Muuronen, M.; Lucas, F.; Sijbesma, R. P.; Tomović, Ž. Catalysis for Isocyanate Trimerization. *ChemCatChem* **2023**, *15*, No. e202201362.
(41) Bahili, M. A.; Stokes, E. C.; Amesbury, R. C.; Ould, D. M. C.; Christo, B.; Horne, R. J.; Kariuki, B. M.; Stewart, J. A.; Taylor, R. L.; Williams, P. A.; Jones, M. D.; Harris, K. D. M.; Ward, B. D. Aluminium-catalysed Isocyanate Trimerization, Enhanced by Exploiting a Dynamic Coordination Sphere. *Chem. Commun.* **2019**, *55*, 7679−7682.
(42) Porosity values and BET surface areas are low compared with other aerogels, for example, silica.[24] However, the use of the term "aerogel" to describe the materials of this study is not associated with any specific set of properties but rather with the fact that it refers to materials coming from wet gels the pore-filling solvent of which was replaced with air using methods that minimize shrinkage: "Aerogel is an open non-fluid colloidal network or polymer network that is expanded throughout its whole volume by a gas, and is formed by the removal of all swelling agents from a gel without substantial volume reduction or network compaction".[43]
(43) Supporting Information of: Leventis, N.; Sadekar, A.; Chandrasekaran, N.; Sotiriou-Leventis, C. Click Synthesis of Monolithic Silicon Carbide Aerogels from Polyacrylonitrile-Coated 3D Silica Networks. *Chem. Mater.* **2010**, *22*, 2790−2803.
(44) Stille, J. K. Step-Growth Polymerization. *J. Chem. Educ.* **1981**, *58*, 862.
(45) Pinto, J.; Solórzano, E.; Rodriguez-Perez, M. A.; De Saja, J. A. Characterization of the Cellular Structure Based on User-Interactive Image Analysis Procedures. *J. Cell. Plast.* **2013**, *49*, 555−575.
(46) Mulik, S.; Sotiriou-Leventis, C.; Churu, G.; Lu, H.; Leventis, N. Cross-Linking 3D Assemblies of Nanoparticles into Mechanically Strong Aerogels by Surface-Initiated Free-Radical Polymerization. *Chem. Mater.* **2008**, *20*, 5035−5046.
(47) Ratke, L.; Rege, A.; Aney, S. The Effect of Particle Necks on the Mechanical Properties of Aerogels. *Materials* **2022**, *16*, 230.
(48) Mohite, D. P.; Larimore, Z. J.; Lu, H.; Mang, J. T.; Sotiriou-Leventis, C.; Leventis, N. Monolithic Hierarchical Fractal Assemblies of Silica Nanoparticles Cross-Linked with Polynorbornene via Romp: A Structure-Property Correlation from Molecular to Bulk through Nano. *Chem. Mater.* **2012**, *24*, 3434−3448.
(49) Leventis, N.; Sotiriou-Leventis, C.; Chandrasekaran, N.; Mulik, S.; Larimore, Z. J.; Lu, H.; Churu, G.; Mang, J. T. Multifunctional Polyurea Aerogels from Isocyanates and Water. A Structure-Property Case Study. *Chem. Mater.* **2010**, *22*, 6692−6710.
(50) Zarr, R. R.; Pintar, A. L. *Standard Reference Materials: SRM 1453, Expanded Polystyrene Board, for Thermal Conductivity from 281 K to 313K*; NIST Special Publication, 2012; 260-175.
(51) Lu, X.; Arduini-Schuster, M. C.; Kuhn, J.; Nilsson, O.; Fricke, J.; Pekala, R. W. Thermal Conductivity of Monolithic Organic Aerogels. *Science* **1992**, *255*, 971−972.

https://doi.org/10.1021/acsapm.3c00882
ACS Appl. Polym. Mater. 2023, 5, 6851−6863